

# MVDR Beamforming for Through-the-Wall Radar Imaging

Yeo-Sun Yoon, *Member, IEEE*, Moeness G. Amin, *Fellow, IEEE* and  
Fauzia Ahmad *Senior Member, IEEE*,

## Abstract

We present high definition imaging for targets behind walls and enclosed structures based on constrained minimization RF multi-sensor processing. Minimum variance distortionless response (MVDR) beamforming is used on both sensor-frequency raw data radar returns and spatial spectrum data, which is obtained by the Fourier transform of the delay and sum beamformer image. We compare both methods for near-field and far-field scenes. The paper considers both cases of known and unknown wall parameters and uses manifold constraints to allow target localization in high-definition imaging in the presence of wall errors. Also, through analyses and simulations, we show how to effectively use the spatial spectrum to improve covariance matrix estimation, and subsequently enhance image quality in the sense of lower sidelobes.

## Index Terms

High resolution radar imaging, MVDR, Through-the-wall radar, Capon Method, Delay-and-sum beamforming

## I. INTRODUCTION

Radio frequency (RF) sensing is the technology of choice in through-the-wall applications as it provides vision into otherwise obscured areas [1]–[7]. Radio frequencies can penetrate through nonmetallic walls and, more importantly, unlike other technologies, RF solutions can be provided at long stand-off distances from the external walls. Through-the-wall radar imaging

Authors are with the Radar Imaging Lab, Center for Advanced Communications, Villanova University, 800 E. Lancaster Ave, Villanova, PA 19085, USA.

This work was supported by ONR under grant no. N00014-07-1-0043.

(TWRI) can be realized by transmitting and receiving wideband signals at multiple locations [8]. The target location can be estimated by using wideband delay-and-sum (DS) beamforming, where a set of delays are applied to align all signal returns corresponding to a hypothesized target location. These returns are then summed and processed by a matched filter to produce an image intensity value at each location. DS beamforming with knowledge of wall characteristics has been extensively examined for TWRI applications [1], [9], [10].

In order to deliver high quality imaging for targets behind walls and in enclosed structures, very large signal bandwidth and array aperture must be used, respectively, to provide high resolutions in down-range and cross-range. Operation logistics and covertness, frequency spectrum management, and system constraints may not permit these requirements to be satisfied. High-definition adaptive schemes can, however, be applied to overcome the limitations of Fourier-based imaging. These schemes not only provide high imaging resolution, but also offer good interference suppression capabilities [11]. Both properties stem from adopting data-dependent radar imaging methods, which are faced with the challenge of estimating the covariance matrix from only a single snapshot. In this regard, multiple virtual snapshots need to be formed from a single data observation by interpolation of the raw data on a rectangular grid [12] or through sub-band processing [13], [14]. An alternative to the data interpolation approach for covariance matrix estimation is to use the 2D spectrum of the image that is generated by a low-resolution image formation algorithm, such as DS beamforming [11], [15].

In this paper, we use minimum variance distortionless response (MVDR) beamforming with a frequency step implementation of a wideband pulse to provide high definition imaging of indoor targets. By high-definition, a high quality image in the sense of lower sidelobes and interference suppression is implied. We apply MVDR beamforming to both the raw frequency-sensor data approach and the beamspace approach. The former is known to result in biased target locations when the scene of interest is located in the near field of the array. Since near field operations are likely to be encountered in urban sensing, estimating the covariance matrix from the spatial spectrum associated with DS beamforming is considered more suitable for TWRI applications. We show, however, that when using beamspace processing, one should only consider the region in the spatial spectrum which corresponds to the target, otherwise virtual snapshots obtained by subarray and subband vectors will not properly correspond to the array manifolds, leading to target image dispersion. Note that the magnitude of the target spatial spectrum follows a ‘sinc’

function behavior, rendering non-constant magnitudes of the elements in the virtual snapshots. It is shown that these fluctuations tend to smooth out due to the averaging process during the covariance matrix estimation. In essence, the target bandwidth in the spatial frequency domain is determined by the target extent in the DS image, which in turn depends on three factors, namely, the radar system resolution, image pixel size, and the location of the beam relative to the antenna array. All of these parameters should be known in advance. Once the target is imaged by the DS beamformer, the corresponding spectrum region can be readily determined.

In the case where the wall characteristics are unknown, the target image from MVDR beamforming can both shift in position and blur in intensity. Autofocusing techniques have been proposed in the context of DS beamforming to overcome the wall impairing effects [16], [17], wherein the effect of wall ambiguities on the target spread and intensity profile is examined, aiming to focus the image. As a secondary effect, the autofocusing techniques also correct for shifts in the locations of the imaged targets. An alternate technique that provides correct locations of stationary targets without the knowledge of wall parameters was proposed in [18]. This technique is also based on DS beamforming, but utilizes the displacement, rather than blurriness, of the imaged targets. It requires the use of a double-viewing operation, where the imaging system is deployed at two different locations. This approach corrects for wall ambiguities by constructing a trajectory of the imaged target locations, using different assumed wall characteristics. Different positions of the imaging system generate different trajectories that intersect at the true target location.

In this paper, we consider high definition imaging with known and unknown walls. For the latter, we analyze the bias in imaged target location due to wall errors beyond that which is discussed in reference [18]. These analyses are then used to construct additional constraints on the MVDR beamformer so as to provide unbiased target locations when imaging with different system views.

The paper is organized as follows. In Section II, through-the-wall radar (TWR) is briefly discussed. In Section III, high-definition radar imaging in the presence of known walls is presented. Section IV and V explain both the raw data approach and the beamspace approach using exact wall parameters, followed by Section VI which shows the processing results of both simulated data and real data measurements. In Section VII, the effect of wall parameter errors on TWRI is analyzed, and a high definition target localization approach in the presence

of unknown walls using two array positions and constrained MVDR beamforming is proposed. In Section VIII, a proof of concept for unknown wall parameters is provided using simulated data. Section IX contains concluding remarks.

## II. THROUGH-THE-WALL RADAR

### A. Signal Model

We consider wideband radar imaging based on monostatic data collection schemes. A single antenna transmits and receives a wideband signal, with desired range resolution, at one location, then moves to the next location to repeat the transmit/receive process until it exhausts all locations, defining the synthesized array aperture. The wideband signal is generated using a stepped-frequency approach in which the transmitter sweeps through the allocated signal bandwidth via a series of narrowband signals of uniformly spaced center frequencies. Let  $N_f$  be the number of narrowband signals and  $N_a$  be the number of antenna locations for data collection. For a scene consisting of  $P$  point targets, the received signal at the  $l$ -th antenna location corresponding to the narrowband transmit waveform of frequency  $f_k$  is given by [15],

$$z(k, l) = \sum_{p=0}^{P-1} \sigma_p \exp\{-j2\pi f_k \tau_{l,p}\} \quad (1)$$

where  $k = 0, \dots, N_f - 1$ ,  $l = 0, \dots, N_a - 1$ ,  $\sigma_p$  is the complex reflection coefficient of the  $p$ -th target,  $\tau_{l,p}$  is the two-way traveling time from the  $l$ -th antenna location to the  $p$ -th target, and

$$f_k = f_0 + k\Delta f, \quad \Delta f = \frac{f_{N_f-1} - f_0}{N_f - 1} \quad (2)$$

where  $f_0$  is the lowest frequency in the desired frequency band and  $\Delta f$  is the frequency step size. In the absence of a wall, the traveling time of the signal is determined by the line-of-sight distance between the antenna and the target. In this case,  $\tau_{l,p}$  is given by,

$$\tau_{l,p} = \frac{2}{c} \sqrt{(x_p - x_l)^2 + (y_p - y_l)^2}, \quad (3)$$

where  $c$  is the speed of light in free-space,  $(x_p, y_p)$  is the location of the  $p$ -th target and  $(x_l, y_l)$  is the  $l$ -th antenna location.

For through-the-wall radar, the signal undergoes attenuation, dispersion, refraction, and a change in speed as it propagates through the wall. As a result, the path emanating from the antenna and reaching the target is no longer line-of-sight. Assuming a homogenous wall of

thickness  $d$  and dielectric constant  $\epsilon$ , the two-way propagation time  $\tau_{l,p}$  from the  $l$ -th antenna to the  $p$ -th target, ignoring the multiple reflections within the wall, is given by [19] (See Fig. 1),

---

Insert Figure 1 here

---

$$\tau_{l,p} = \frac{2g_1}{c} + \frac{2g_2\sqrt{\epsilon}}{c} + \frac{2g_3}{c}, \quad (4)$$

where

$$g_1 = \frac{h_1}{\cos \phi}, \quad g_2 = \frac{d}{\cos \theta}, \quad g_3 = \frac{h_2}{\cos \phi}, \quad \sqrt{\epsilon} \sin \theta = \sin \phi, \quad (5)$$

with

$$(a - h_1 \tan \phi)^2 + (h_2 + d)^2 = g_2^2 + g_3^2 - 2g_2g_3 \cos(\pi + \theta - \phi). \quad (6)$$

The variables  $h_1$ ,  $h_2$ , and  $a$  are defined in Fig. 1, and are functions of the antenna and target locations. The variables  $\theta$  and  $\phi$  represent the angles of incidence and refraction, respectively. Note that the above equation is most applicable to the case of homogeneous wall in which the signal propagates at a constant speed. It is further noted that in the signal model of eq. (1), the wall reflections, resulting from a mismatch in the material properties at the air-wall-air interface, are assumed to have been mitigated using effective wall return removal techniques such as those recently proposed in [17], [20], [21].

### B. Delay-and-Sum Beamforming

An image of the scene can be obtained by using wideband delay-and-sum beamforming, where a set of delays are applied to align all signal returns corresponding to a presumed target location [1]. The complex image value  $B(x, y)$  at pixel  $(x, y)$  is obtained by weighting and summing the delayed signals,

$$B(x, y) = \frac{1}{N_f N_a} \sum_k \sum_l w(k, l) z(k, l) \exp\{j2\pi f_k \tau_{l,(x,y)}\} \quad (7)$$

Here,  $w(k, l)$  is the weighting function and  $\tau_{l,(x,y)}$  is the two-way propagation time of the signal from the  $l$ -th antenna to the beamforming point  $(x, y)$ .

### III. HIGH-DEFINITION THROUGH-THE-WALL RADAR IMAGING

High-definition, here, implies high-quality imagery in the sense of low sidelobes and interference suppression with resolution dictated by the size of the synthesized array aperture. In applying these methods for imaging through walls, the data covariance matrix must first be estimated [22], [23]. Estimation of the covariance matrix is performed in many applications through time-averaging where data snapshots are collected over an observation period. In most of the radar applications, however, only a single snapshot is possible, and as such, data preprocessing to reduce the estimation variance becomes necessary. In [13] and [14], multiple snapshots are obtained by sub-array and sub-band processing of the data. The data is first partitioned into multiple overlapping subsets. Delay-and-sum beamformed images, obtained by independent processing of these different data subsets, are then used to estimate the covariance matrix. The shortcoming of this approach is that only a limited number of low-resolution images are used. The virtual snapshots, which allow covariance matrix estimation through averaging, can be formed with the 2D spatial spectrum of the scene  $g(s, u)$  [12], [15]. It is noted that the spatial spectrum must first be preprocessed to remove the effect of the weighting  $w(k, l)$  applied in DS image formation. However, this is not a straightforward process due to the finite number of antenna locations and frequencies. Therefore, in the following analysis and ensuing sections, we assume that  $w(k, l) = 1$  for all  $k$  and  $l$ . For a single point target located at  $(x_0, y_0)$ ,

$$g(s, u) = \sigma_0 \exp\{-j2\pi(sx_0 + uy_0)\}, \quad (8)$$

where  $\sigma_0$  is the reflection coefficients of the target. It is noted that the information constraining target locations is contained in the phase of the 2D spatial spectrum. In practice, only part of the spatial spectrum will be available. Define a  $K \times L$  matrix,

$$\mathbf{G}_{k,l} = \begin{bmatrix} g(k, l) & \cdots & g(k, l + L - 1) \\ g(k + 1, l) & \cdots & g(k + 1, l + L - 1) \\ \vdots & \ddots & \vdots \\ g(k + K - 1, l) & \cdots & g(k + K - 1, l + L - 1) \end{bmatrix}, \quad (9)$$

where  $g(k, l) := g(s_k, u_l)$  for  $s_k = s_0 + k\Delta s$ ,  $u_l = u_0 + l\Delta u$ .  $s_0$  and  $u_0$  represent the lowest available frequencies, and  $\Delta s$  and  $\Delta u$  are the frequency steps. The virtual snapshots are defined by

$$\mathbf{g}_{k,l} = \text{vec}\{\mathbf{G}_{k,l}\}. \quad (10)$$

In the above equation,  $\text{vec}\{\}$  is the vectorizing operator which stacks all the matrix columns into one vector. It is convenient to define an array manifold vector  $\mathbf{a}(x, y)$ ,

$$\mathbf{a}(x, y) = \boldsymbol{\alpha}(x) \otimes \boldsymbol{\beta}(y), \quad (11)$$

where  $\otimes$  denotes Kronecker product and

$$\boldsymbol{\alpha}(x) = [e^{j2\pi s_0 x} \ e^{j2\pi s_1 x} \ \dots \ e^{j2\pi s_{K-1} x}]^H, \quad (12)$$

$$\boldsymbol{\beta}(y) = [e^{j2\pi u_0 y} \ e^{j2\pi u_1 y} \ \dots \ e^{j2\pi u_{L-1} y}]^H, \quad (13)$$

Then, the relationship between  $\mathbf{g}_{k,l}$  and  $\mathbf{a}(x, y)$ , for  $x = x_0$  and  $y = y_0$ , is

$$\mathbf{g}_{k,l} = \sigma_0 \exp\{-j2\pi(k\Delta s x_0 + l\Delta u y_0)\} \mathbf{a}(x_0, y_0). \quad (14)$$

Accordingly, the covariance matrix can be estimated as,

$$\hat{\mathbf{R}} = \sum_k \sum_l \mathbf{g}_{k,l} \mathbf{g}_{k,l}^H, \quad (15)$$

where the superscript  $H$  denotes conjugate transpose. When there is  $P$  point targets, the structure of the covariance matrix is

$$\hat{\mathbf{R}} = \begin{bmatrix} \mathbf{a}^H(x_0, y_0) \\ \vdots \\ \mathbf{a}^H(x_{P-1}, y_{P-1}) \end{bmatrix} \begin{bmatrix} \gamma_0 & 0 & \dots & 0 \\ 0 & \gamma_1 & & \\ \vdots & & \ddots & 0 \\ 0 & \dots & 0 & \gamma_{P-1} \end{bmatrix} \begin{bmatrix} \mathbf{a}(x_0, y_0) & \dots & \mathbf{a}(x_{P-1}, y_{P-1}) \end{bmatrix} + \boldsymbol{\Sigma} \quad (16)$$

where  $\boldsymbol{\Sigma}$  is the covariance matrix of noise and,

$$\gamma_p = \sigma_p \sum_k \sum_l \exp\{-j2\pi(k\Delta s x_p + l\Delta u y_p)\} \quad (17)$$

for  $p = 0, \dots, P-1$ . Note that  $\mathbf{a}(x, y)$  are independent of  $\mathbf{a}(x', y')$  when  $x \neq x'$  or  $y \neq y'$ .

Once the covariance matrix is estimated, data-dependent imaging approaches can be applied to obtain a high-definition image of the scene. MVDR beamforming can provide both RCS estimates and high-definition imaging [23]. The image pixel value corresponding to Capon estimator, which is singly constrained MVDR, is

$$I(x, y) = \min_{\mathbf{w}} \mathbf{w}^H \hat{\mathbf{R}} \mathbf{w} \text{ subject to } \mathbf{w}^H \mathbf{a}(x, y) = 1, \quad (18)$$

There are mainly two approaches, discussed below, to estimate the spatial spectrum necessary to apply (18), one is a raw data-based approach and the other is a beamspace-based approach.

#### IV. RAW DATA-BASED APPROACH

---

Insert Figure 2 here

---

When the far-field approximation is valid [12], the received signal  $z(k, l)$  in (1) can be considered as a sample of the spatial spectrum, assuming that the antenna beamwidth is sufficiently wide to cover the entire scene of interest. Then,  $z(k, l)$  can be approximated by,

$$z(k, l) \approx \sum_{p=0}^{P-1} \sigma_p \exp\left\{-j \frac{4\pi f_k}{c} (r_l + x_p \cos \phi_l - y_p \sin \phi_l)\right\} \quad (19)$$

where  $r_l$  is the length of the signal path between the  $l$ -th antenna and the center of the scene in the presence of the wall,  $(x_p, y_p)$  is the location of the  $p$ -th target, and  $\phi_l$  is the angle of refraction corresponding to the signal path from the  $l$ -th antenna to the center of the scene (See Fig. 2). Note that the target location  $(x_p, y_p)$  is in the image domain with the center of the scene at  $(0, 0)$ . For small values of  $\phi_l$ , which is typically the case in the far-field,  $\cos \phi_l \approx 1$  and  $\sin \phi_l \approx \phi_l$ . Under these assumptions and after compensating for the target-independent phase term, equation (19) can be written as,

$$z(k, l) = g(s, u)|_{s=2f_k/c, u=2f_k\phi_l/c}, \quad (20)$$

where

$$g(s, u) = \sum_{p=0}^{P-1} \sigma_p \exp\{-j2\pi s x_p + j2\pi u y_p\}. \quad (21)$$

The range  $r_l$  and the angle  $\phi_l$  vary from one antenna location to the other and should be computed for each  $l$  using air-wall-air propagation path. Equation (20) represents a non-uniformly sampled version of the two-dimensional spatial spectrum of the scene. With 2D interpolation, uniformly sampled representation can be obtained, permitting a single snapshot estimation of the covariance matrix, as discussed in the previous section. In this case, the covariance matrix estimate  $\hat{\mathbf{R}}$  is given by,

$$\hat{\mathbf{R}} = \sum_k \sum_l \mathbf{g}_{k,l} \mathbf{g}_{k,l}^H \quad (22)$$



where  $\mathbf{g}_{k,l}$  is a virtual snapshot,  $\mathbf{g}_{k,l} = \text{vec}\{\hat{\mathbf{Z}}_{k,l}\}$ , and  $\hat{\mathbf{Z}}_{k,l}$  is a  $K \times L$  matrix whose elements are the two-dimensional spatial spectrum ,

$$\hat{\mathbf{Z}}_{k,l} = \begin{bmatrix} \hat{z}(k, l) & \cdots & \hat{z}(k, l + L - 1) \\ \hat{z}(k + 1, l) & \cdots & \hat{z}(k + 1, l + L - 1) \\ \vdots & \ddots & \vdots \\ \hat{z}(k + K - 1, l) & \cdots & \hat{z}(k + K - 1, l + L - 1) \end{bmatrix}. \quad (23)$$

In the above equation,  $\hat{z}(k, l)$  is an interpolated version of  $z(k, l)$  with uniformly sampled spatial frequencies. Any interpolation method, such as linear, polynomial, or spline, can be used. For the simulations in Section VI, we have used the linear interpolation method for simplicity. The frequency steps  $\Delta s$  and  $\Delta u$  are the same as the interpolation intervals. As shown in [15], the spatial frequencies  $s$  and  $u$  are bounded by,

$$f_0 \leq s \leq f_{N_f-1} \cos \phi_{N_a-1}, \quad s \sin \phi_0 \leq u \leq s \sin \phi_{N_a-1}. \quad (24)$$

---

Insert Figure 3 Here

---

The above boundaries do not conform to a rectangle. Figure 3 shows the largest rectangle that fits the area defined by the above boundaries. The number of discrete samples in that spectrum depends on the interpolation interval, which can be arbitrary chosen. However, in order to minimize the interpolation errors, there must be at least one data sample between interpolation points. Once the number of samples in the spatial spectrum is decided, the sub-matrix size ( $K \times L$ ) can be determined. Large  $KL$  yields high-resolution, but, at the same time, limits the number of snapshots. If the number of virtual snapshots is less than the dimension of the virtual snapshots, diagonal loading is necessary to render the covariance matrix estimate nonsingular [11]. Throughout the simulations in this paper, we used 60% of the spectrum samples for  $K$  and  $L$ .

## V. BEAMSPACE-BASED APPROACH WITH KNOWN WALL

### A. Obtaining the two-dimensional spatial spectrum

Beamspace (BS) processing uses the 2D spatial spectrum of the delay-and-sum beamformed image of the scene [11], [15]. This method was originally proposed by Benitz in [11], and

analyzed in detail in [15]. The scene of interest with  $P$  point targets can be represented by the following equation,

$$f(x, y) = \sum_{p=0}^{P-1} \sigma_p \delta(x - x_p, y - y_p) \quad (25)$$

where  $\delta(\cdot)$  is the Dirac-delta function. The discrete version of  $f(x, y)$  on an  $M \times N$  rectangular grid can be obtained by DS beamforming. That is,

$$f[m, n] = f(x_m, y_n) \approx B(m, n), \quad (26)$$

where  $(x_m, y_n)$  for  $m = 0, \dots, M-1$  and  $n = 0, \dots, N-1$  are uniformly spaced beamforming points that span the scene of interest and  $B(m, n)$  is given by eq. (7), reproduced below for convenience,

$$B(m, n) = \frac{1}{N_f N_a} \sum_k \sum_l w(k, l) z(k, l) \exp\{j2\pi f_k \tau_{l, (x_m, y_n)}\}. \quad (27)$$

Note that eq. (27) is valid for near-field as well as far-field processing. The approximation in eq. (26) is valid for moderate array size and bandwidth. For the approximation to become an exact equality, the array length as well as the signal bandwidth should be infinite.

The two-dimensional spatial spectrum of the scene  $F[k_x, k_y]$  can be obtained by applying the two-dimensional discrete Fourier transform,

$$F[k_x, k_y] = \sum_{m=0}^{M-1} \sum_{n=0}^{N-1} f[m, n] \exp\{-j\frac{2\pi m k_x}{M} - j\frac{2\pi n k_y}{N}\}, \quad (28)$$

where  $k_x = 0, \dots, M-1$  and  $k_y = 0, \dots, N-1$ . In this respect, the target location can be obtained by parameter estimations based on  $F[k_x, k_y]$ . The covariance matrix estimate  $\hat{\mathbf{R}}$  can be provided using virtual snapshots in a similar way as in the raw data-based approach. In this case, the new steering vector  $\mathbf{a}(m, n)$  is given by,

$$\mathbf{a}(m, n) = \boldsymbol{\alpha}(m) \otimes \boldsymbol{\beta}(n), \quad (29)$$

where

$$\begin{aligned} \boldsymbol{\alpha}(m) &= [1 \ e^{j2\pi m/M} \ \dots \ e^{j2\pi(K-1)m/M}]^H, \\ \boldsymbol{\beta}(n) &= [1 \ e^{j2\pi n/N} \ \dots \ e^{j2\pi(L-1)n/N}]^H. \end{aligned}$$

Note that no interpolation is necessary for beamspace approach, which is advantageous since interpolation produces data errors. The number of samples in the spatial spectrum is the same as

the number of beams. The number of beams is determined by the pixel size of the image. If this space is smaller than the radar resolution, a point target will be represented by multiple pixels. In this case, the corresponding spatial spectrum will tend to be localized. On the other hand, if the space is larger than the resolution, the mainlobes of DS beamformer will not effectively overlap, and targets located between beams will likely be missed. It should also be mentioned that since the beamforming points do not necessarily match the target locations, there might be target displacements or reduction in intensity in the high-definition image caused by a combination of large (strong) and small (weak) targets in the scene. In this paper, we use DS image with pixels smaller than the system resolution and consider, for covariance matrix estimation, the area where most of the energy of target is localized, as discussed below.

### B. Location of the target in the spatial spectrum

Let  $\delta x$  and  $\delta y$  be the space between beams along down-range and cross-range, respectively. Suppose that,

$$\delta x = \mu_x \rho_x, \quad \delta y = \mu_y \rho_y, \quad (30)$$

where  $\rho_x$  and  $\rho_y$  are the respective cross-range resolution and down-range resolution. The constants  $\mu_x$  and  $\mu_y$  denote how much the signal is oversampled in the image domain. The equivalent time interval  $\delta T$  between two beams and the corresponding sampling frequency  $f_s$  are,

$$\delta T = \frac{2\delta x}{C}, \quad f_s = \frac{1}{\delta T} = \frac{C}{2\delta x}. \quad (31)$$

For the frequency bandwidth  $f_B$ , the down-range resolution is  $\rho_x = C/2f_B$ , and the sampling frequency is,

$$f_s = \frac{C}{2\mu_x(C/2f_B)} = \frac{f_B}{\mu_x}. \quad (32)$$

Note that if  $\mu_x \leq 1$ , the space between beams is smaller than the system resolution, and the spectrum will be supported by only  $2\pi\mu_x$ , the location of which is determined by both the sampling frequency and the signal bandwidth.

To explain the support region for cross-range, we consider a point target located at the boresight of the array. Suppose that the pixel size along cross-range is less than the system resolution

( $\mu_y < 1$ ), so the point target is represented by  $2E + 1$  pixels. Then, the corresponding 2D discrete spatial spectrum is

$$F[k_x, k_y] = \exp\{-j2\pi k_x m_0/M\} \exp\{-j2\pi k_y n_0/N\} \frac{\sin \frac{2\pi k_y (E+0.5)}{N}}{\sin \frac{\pi k_y}{N}}, \quad (33)$$

for  $k_x = 0, \dots, M-1$ ,  $k_y = 0, \dots, N-1$ , and  $(m_0, n_0)$  is the point target location. The magnitude of the spectrum is determined by the sine term. The effective width of the spectrum is determined by half of the distance between two zeros of the numerator,

$$K = \frac{M}{2(E+0.5)} = M\mu_y. \quad (34)$$

In the above equation, we have used

$$(2E+1)\delta y = (2E+1)\mu_y r_y = r_y. \quad (35)$$

---

Insert Figure 4 & 5 Here

---

Figure 4 shows the location of the spectrum in the normalized 2D spatial frequency domain. Note that the above equation is for the case when the target is extended parallel to the array. When the target is off boresight, however, the point target in the DS image will be extended perpendicular to the radial line from the center of the array. In this case, the spectrum will be rotated corresponding to the ‘squint’ angle  $\theta$  (See Fig. 5(a)). When the signal is rotated, its spectrum is also rotated in the same way, per the following equations:

$$f(x, y) \rightarrow f(x \cos \theta + y \sin \theta, -x \sin \theta + y \cos \theta) \quad (36)$$

$$F(f_x, f_y) \rightarrow F(k_x \cos \theta + k_y \sin \theta, -k_x \sin \theta + k_y \cos \theta). \quad (37)$$

Although the target is rotated around the center of the array, not the center of the axis, the above equation is still valid up to a phase. Figure 5(b) shows the spatial spectrum when the target is located at off-boresight angle,  $\theta$ . In Fig. 5(b), most of the power is located in the shaded region, which corresponds to the mainlobe of the target spatial spectrum.

---

— Insert Figure 6 here —

---

We note that the magnitude of the target spatial spectrum is not constant due to the presence of the 'sine' term in eq. (33), resulting in variations in the magnitude of the elements in the virtual snapshots. This magnitude profile causes a mismatch with the assumed constant-amplitude steering vector in eq. (29). However, these magnitude fluctuations tend to smooth out to approximately a constant due to the averaging process during the estimation of the covariance matrix, as shown in Fig. 6, rendering the constant-amplitude steering vector model applicable. Figure 6 depicts the magnitude of the elements of several virtual snapshots (dotted curves) for the case of a single point target with  $\mu_y = 1/16$  and  $\mu_x = 1/4$ . The solid curve in Fig. 6 represents the magnitude of the elements of the steering vector after the averaging process in covariance matrix estimation. The magnitudes are normalized so that the mean magnitude is equal to unity. The standard deviation of the virtual-snapshot magnitudes varies from 0.16 to 0.65, whereas that of the steering vector is 0.09.

### C. Effective covariance matrix estimation

---

— Insert Figure 7 here —

---

As discussed in the previous section, the effective spatial spectrum of the target is confined to a limited region of the Fourier transform of the DS image. Therefore, only the part where the target exists in the spatial frequency domain should be used for covariance matrix estimation. One simple way to tile the spatial spectrum corresponding to target positions in the image is to divide the scene of interest into two parts like mosaic: the positive  $\theta$  part and the negative  $\theta$  part. Figure 7 shows the divided scene and the corresponding parts in the spatial spectrum. Two tiles are overlapped in the center to avoid missing targets located at the boundary. The amount of overlap can be determined by  $\mu_y$ . The shaded are represents the region where most of the target spectrum is localized. Outside this region, the spectrum is highly attenuated and

should be avoided in estimating the covariance matrix, as demonstrated later by a simulation example. As a result, two covariance matrices will be considered. Each covariance matrix contains information about the targets in the corresponding image region, and as such will be used in MVDR beamforming for that region. In this way, the covariance matrix for positive  $\theta$ -region will provide the image for one side and the one for negative  $\theta$ -region will provide the image for the other side.

Note that the cross-range resolution depends on the radial distance between the beamforming point and the center of the array. In order to include all target information in a tile, the size of the sub-matrix should be determined according to the cross-range resolution of the farthest target and the maximum off-boresight angle  $\theta_{max}$  in the tile.

## VI. SIMULATION RESULTS OF KNOWN WALL DATA

In order to compare the above two approaches, we used two synthesized data sets, one for near-field and one for far-field. In both cases, the scene of interest is  $4\text{m} \times 4\text{m}$ . In the near-field case, the distance from the wall to the center of the scene is 6m. The length of the linear array is 1.2m with 61 elements and the bandwidth of the signal is 1GHz (2GHz - 3GHz). In the far-field case, the distance to the center of the scene is 25m, and a 5m long array consisting of 63 elements is used with the same frequency band as the near-field scene. The down-range resolution for both scenes is 0.15m. The cross-range resolution at the center frequency and at the center of the scene is 0.6m for both cases. A 15 inch thick wall with 7.0 dielectric constant, typical of concrete, is located at 0m in down range. Assuming known wall parameters, the wall effects are compensated for before applying the high-definition imaging algorithms. The pixel size of the DS image is  $0.0375 \times 0.0375\text{m}$  which is one fourth of the down-range resolution ( $\mu_x = 1/4$ ) and 1/16 of the cross-range resolution ( $\mu_y = 1/16$ ). The parameter  $K$  and  $L$  are chosen as 13 and 6 respectively. The value of  $L$  is the product of  $\mu_y$  and the total number of columns ( $107/16 \approx 6.7$ ) in the DS image.

---

Insert Figure 8,9,10,11 Here

---

In all the figures in this section as well as the following sections, all image values are in dB units with the maximum level normalized to 0dB. Figure 8 shows the processing results using

DS beamformer. The left figure is the far-field scene and the right figure is the near-field scene. Two targets are shown at their locations which are marked by circles. Since the wall effects are perfectly compensated for, the targets appear at the correct locations. Figure 9 shows the same scenes obtained by the raw data-based Capon. As expected, Capon beamforming provides high-definition imaging. In the near-field case, however, even with the wall effects are properly accounted for, there are biases in the target locations in the raw data approach which is due to far-field approximation. Figure 10 is the beamspace-based Capon image which, compared to Fig. 9, shows images of high resolution and without any biases, even in the near field. Figure 11(a) shows the beamspace-based Capon image when all the spatial spectrum is used for covariance matrix estimation. It is clear that the quality of the image is worse than Fig. 10, which only used the target spatial spectrum support region, depicted in Fig. 11(b). The straight lines denote the area which is processed to image the left half of the scene (negative  $\theta$ ), where the targets are located.

---

Insert Figure 12 Here

---

Figures 12(a) and 12(b) show the spatial leakage patterns for the DS and beamspace Capon beamformers at the beamforming point is at  $(-0.8, 5.5)\text{m}$  which coincides with the location of one of the two targets. The advantage of the Capon beamformer over the DS beamformer is evident. The DS beamformer has a high sidelobe at the second target, located at  $(-0.988, 6.512)\text{m}$ , while the Capon beamformer places a null there, minimizing the interference from the second target, thereby providing a more accurate estimate of the target Radar cross-section (RCS).

---

Insert Figure 13 Here

---

Real experiment data set is also tested. A wideband synthetic aperture through-the-wall radar system was set up in the Radar Imaging Lab at Villanova University. A stepped-frequency CW signal, consisting of 501 frequency steps of size 5 MHz, covering the 1-3 GHz band was chosen for imaging. An Agilent network analyzer, model ENA 5071B, was used for signal synthesis and data collection. A horn antenna, model ETS-Lindgren 3164-04, with an operational bandwidth from 0.7 to 6 GHz, was used as the transceiver and mounted on a Field Probe Scanner to

synthesize a 67-element monostatic line array with an inter-element spacing of 0.018m (0.735in). A 3.0m x 2.4m x 0.05m (10ft x 8ft x 2in) plywood wall segment, with a dielectric constant of 2.5, was constructed. The wall was positioned 1.0m (40in) downrange from the antenna feed. The scene has one vertical dihedral at a height of about 1.44m (56.75in). Each face of the dihedral is 0.39m (15.5in) by 0.28m (11in). The height of the array was fixed at the same height as the dihedral. Empty scene measurements were also made with only the wall present in the test area. These measurements were coherently subtracted from the target scene and the resulting data sets were used for generating the images. Figure 13 shows the DS image and the beam-space Capon image. Capon beamforming of real data provides a better image than DS beamforming in the sense of reducing the sidelobes, even though the experimental data set is corrupted by noise, multipath and/or reflections, and the dihedral is not a point target unlike the previous synthesized data set.

## VII. BEAMSPACE MVDR WITH UNKNOWN WALL

### A. Effect of Wall Parameter Errors

---

Insert Figure 14 Here

---

Through-the-wall radar imaging with assumed wall parameters, which are different from their true values, will result in image degradation. Figure 14 shows the DS images of the simulated two-target scene of Section VI under 10% and 20% error in the wall parameters. Although two targets are clearly seen, their locations are biased and the amount of bias is proportional to the errors. Since the beam-space approach is based on the DS image, the beam-space MVDR will also result in the biased target locations. Image degradation is also witnessed for the method based on interpolated raw data as it causes errors in  $r_l$  in (19). As such, the received signals will not be properly aligned at the center of the scene and any high-definition methods based on the corresponding covariance matrix estimate will suffer.

---

Insert Figure 15 Here

---



Let  $\Delta d$  and  $\Delta\epsilon$  be the errors in the wall thickness and dielectric constant, respectively. Due to the wall parameter errors, the target in the DS image will be located at point  $q$  instead of its true location  $p$ , as shown in Fig. 15 [18]. Let  $\Delta x$  and  $\Delta y$  be the biases in the down-range and cross-range, respectively. In [18], closed form expressions for  $\Delta x$  and  $\Delta y$  are derived for bistatic operation with the transmitter and the receiver symmetrically distributed about the target location. For monostatic operation, the condition of symmetry is no longer valid. Further, in [18] only an error in one wall parameter is considered. Below, we present the analysis for the monostatic synthetic aperture case and describe  $\Delta x$  and  $\Delta y$  in terms of  $\Delta d$ ,  $\Delta\epsilon$ , antenna location, and target location.

Let  $g_f = g_1 + g_3$  and  $g_w = g_2$  be, respectively, the path in the free space and inside the wall, when using the true wall parameters, as depicted in Fig. 1. The two-way propagation time associated with point  $p$  is

$$\tau = 2(g_f/c + g_w\sqrt{\epsilon}/c) = 2\left(\frac{h_1 + h_2}{c \cos \phi} + \frac{d\sqrt{\epsilon}}{c \cos \theta}\right) \quad (38)$$

Denote  $\hat{g}_f$  and  $\hat{g}_w$  as the corresponding paths when using the estimated wall parameters ( $d + \Delta d, \epsilon + \Delta\epsilon$ ). In this case, the round trip time for the point  $q$  is,

$$\begin{aligned} \hat{\tau} &= 2(\hat{g}_f/c + \hat{g}_w\sqrt{\epsilon + \Delta\epsilon}/c) \\ &= 2\left(\frac{h_1 + h_2 - \Delta x - \Delta d}{c \cos \hat{\phi}} + \frac{(d + \Delta d)\sqrt{\epsilon + \Delta\epsilon}}{c \cos \hat{\theta}}\right). \end{aligned} \quad (39)$$

In the above two equations, we have used the following equalities (See Figure 15).

$$\hat{g}_f \cos \hat{\phi} = h_1 + h_2 - \Delta x - \Delta d, \quad g_f \cos \phi = h_1 + h_2 \quad (40)$$

$$\hat{g}_w \cos \hat{\theta} = d + \Delta d, \quad g_w \cos \theta = d \quad (41)$$

In order for the imaged target to appear at point  $q$ , we require  $\tau = \hat{\tau}$ , and obtain the condition

$$\frac{h_1 + h_2 - \Delta x - \Delta d}{\cos \hat{\phi}} + \frac{\sqrt{\epsilon + \Delta\epsilon}(d + \Delta d)}{\cos \hat{\theta}} = \frac{h_1 + h_2}{\cos \phi} + \frac{\sqrt{\epsilon}d}{\cos \theta} \quad (42)$$

Similarly,

$$\hat{g}_f \sin \hat{\phi} + \hat{g}_w \sin \hat{\theta} = g_f \sin \phi + g_w \sin \theta - \Delta y \quad (43)$$

Substituting eqs. (40) - (41) into eq. (43),

$$\begin{aligned} &(h_1 + h_2 - \Delta x - \Delta d)\frac{\sin \hat{\phi}}{\cos \hat{\phi}} + (d + \Delta d)\frac{\sin \hat{\theta}}{\cos \hat{\theta}} \\ &= (h_1 + h_2)\frac{\sin \phi}{\cos \phi} + \frac{d \sin \theta}{\cos \theta} - \Delta y \end{aligned} \quad (44)$$

If we assume  $b \gg a$  (See Fig. 15), we can approximate  $\hat{\theta} \approx \theta$  and  $\hat{\phi} \approx \phi$ . From eq. (42),

$$\frac{\Delta x}{\cos \phi} = -\frac{\Delta d}{\cos \phi} + \frac{\sqrt{\epsilon + \Delta\epsilon}(d + \Delta d)}{\cos \theta} - \frac{d\sqrt{\epsilon}}{\cos \theta} \quad (45)$$

Accordingly,

$$\Delta x = d\epsilon \frac{\tan \theta}{\tan \phi} \left\{ \sqrt{1 + \frac{\Delta\epsilon}{\epsilon}} \left( 1 + \frac{\Delta d}{d} \right) - 1 \right\} - \Delta d \quad (46)$$

From equation (44),

$$(\Delta x + \Delta d) \tan \phi - \Delta d \tan \theta = \Delta y \quad (47)$$

Therefore,

$$\Delta y = d \tan \theta \left[ \epsilon \left\{ \sqrt{1 + \frac{\Delta\epsilon}{\epsilon}} \left( 1 + \frac{\Delta d}{d} \right) - 1 \right\} - \frac{\Delta d}{d} \right]. \quad (48)$$

---

Insert Figure 16 Here

---

We note that the expressions for  $\Delta x$  and  $\Delta y$  are a function of the antenna location. However, when the array length is short relative to the target range, the center of the array can be used to determine the expressions for  $\Delta x$  and  $\Delta y$ . In this case, the two values can be considered independent of antenna locations. Figure 16 shows the bias in the target location as the wall thickness error  $\Delta d$  varies from  $-20\%$  to  $20\%$  ( $d = 0.38\text{m}$ ) and the dielectric constant error  $\Delta\epsilon$  also varies between  $-20\%$  and  $20\%$  ( $\epsilon = 7.0$ ). A  $1.2\text{ m}$  long array located between  $-0.6\text{m}$  and  $0.6\text{m}$  in cross-range and at  $-1\text{m}$  in down-range was used for imaging. The wall is located at  $0\text{ m}$  in down-range. The crosses denote the target locations in the DS image obtained by numerical simulation and the dots denote those calculated by eqs. (46) and (48). The circle represents the true target location, which is  $(-0.5, 6)\text{m}$ . Although the analytically derived biases do not exactly match the simulated biases, they show the same overall trend, captured by the orientation of the biases. The line that passes through both the center of the array and the true target location is also shown in Fig. 16. Extensive simulation results have shown that if we draw the smallest ellipse that includes all the target biases, then the slope of the main axis of the minimum area

ellipse is very close to the slope of the bias defined by  $\Delta y/\Delta x$ ,

$$\begin{aligned}\tan \phi_b &= \frac{\Delta y}{\Delta x} \\ &= \frac{\tan \theta \tan \phi \left[ \epsilon \left\{ \sqrt{1 + \frac{\Delta \epsilon}{\epsilon}} \left( 1 + \frac{\Delta d}{d} \right) - 1 \right\} - \frac{\Delta d}{d} \right]}{\epsilon \tan \theta \left\{ \sqrt{1 + \frac{\Delta \epsilon}{\epsilon}} \left( 1 + \frac{\Delta d}{d} \right) - 1 \right\} - \Delta d \tan \phi}.\end{aligned}$$

---

Insert Figure 17 Here

---

Denote  $\phi_c$  as the angle between the point  $p$  and the center of the array. Then,

$$\begin{aligned}\tan \phi_c &= \frac{(h_1 + h_2) \tan \phi + d \tan \theta}{h_1 + h_2 + d} \\ &= \tan \phi + \frac{d}{b} (\tan \theta - \tan \phi) \\ &= \beta \tan \theta + (1 - \beta) \tan \phi\end{aligned}\tag{49}$$

where  $\beta = d/b$  is the ratio of the wall thickness to the down-range. If desired, the value of  $\tan \phi_b$  can be numerically computed for each pixel of the scene and tabulated prior to system operation. However, Fig. 17 shows the numerically computed difference between the angles  $\phi_c$  and  $\phi_b$ , when  $d = 0.38\text{m}$ ,  $\Delta d = 0.038\text{m}$ ,  $\epsilon = 7.0$ , and  $\Delta \epsilon = 0.7$  for various values of  $\phi_c$  and range. The figure shows that the difference in angle is proportional to  $\phi_c$  as expected. Note that the divergences of the plot from a line are due to the fact that the approximations  $\hat{\theta} \approx \theta$  and  $\hat{\phi} \approx \phi$  in deriving eqs. (46) and (48) are not valid for the chosen simulation parameters. When the scene of interest is far from the array and its width is small, then it is possible to approximate  $\phi_b$  as  $\phi_c$  since  $\phi_c$  is small. The angle  $\phi_c$  will be used as a direction of biases in the MVDR beamformer described in the next section.

### B. Multiple linear constrained MVDR using Two Arrays

In urban sensing applications, buildings may have up to four approachable walls, one on each side. Collecting separate data sets from different ‘view angles’ or ‘views’ has several advantages [24]. For example, multiple data sets can be used coherently to obtain more information about the targets for recognition or clutter suppression. It can also be used to detect targets which are masked by other objects or clutter from one view. In this section, we use two such data

sets to obtain the targets' true locations in the presence of wall parameter ambiguities in the context of MVDR beamforming. According to the analysis in the previous section, the biases due to wall parameter errors are dependent on the 'view angle' of the array which changes with the array location. Accordingly, the imaged target will be displaced to different locations as the position of the imaging system is changed. This property was originally used in [18] to locate the targets using DS beamforming and extensive data post-processing. Here, we utilize the same property, but with a simpler approach in which the optimal weights of the MVDR beamforming are computed only once, according to expected target displacement under wall errors. MVDR beamforming, described below, is used to broaden the mainlobe of the beamformer in order to retain radar returns from around the beamforming point. The extended mainlobes will intersect at the true target location when the MVDR images corresponding to the two different array positions are simultaneously considered or fused (See Fig. 18). Clearly, this intersection becomes more visible for distinct view angles and in the presence of small number of targets.

---

Insert Figure 18 Here

---

The MVDR beamformer is defined as

$$\min_w \mathbf{w}^H \mathbf{R} \mathbf{w} \text{ subject to } \mathbf{B}^H \mathbf{w} = \mathbf{c} \quad (50)$$

which is an optimization problem with multiple constraints [25]. The matrix  $\mathbf{B}$  and  $\mathbf{c}$  represent the constraint set. For the Capon beamformer, described earlier in eq. (18),

$$\mathbf{B} = \mathbf{a}(m, n), \quad (51)$$

$$\mathbf{c} = 1, \quad (52)$$

where  $(m, n)$ , in the underlying problems, is the  $mn$ -th pixel in the image. By choosing  $\mathbf{B}$  and  $\mathbf{c}$ , one can obtain a variety of linear constraints to the beamformer. For the TWRI problem, one should choose  $\mathbf{B}$  and  $\mathbf{c}$  that deal best with wall parameter errors. The goal is to find a compact region in the  $x$ - $y$  (image) plane that includes all possible target displacement positions, then define the constraint set  $(\mathbf{B}, \mathbf{c})$  which ensures that the target intensity in that region is not compromised under optimization.

As shown in Section VII-A and also in [18], the bias in target location tends to be distributed directionally along a straight line. Therefore, by extending the width of the mainlobe of the MVDR beamformer along that line, it is possible to include the target displacements in the mainlobe. One method to achieve this objective is to apply derivative constraint (DC), which is a well-known technique for mainlobe flatness [25]. The derivative constraints are,

$$\mathbf{B} = [\mathbf{a}(m, n) \quad \nabla \mathbf{a}(m, n) \cdot \mathbf{v}_{m,n}], \quad \mathbf{c} = \begin{bmatrix} 1 \\ 0 \end{bmatrix}, \quad (53)$$

where  $\mathbf{v}_{m,n}$  is a unit vector whose direction is the same as that of the target bias at  $(m, n)$ . These constraints would cause the mainlobe of the MVDR beamformer to be broadened along the direction of the bias and, as such, the MVDR Beamformer will not significantly reduce, or cancel, the target radar cross-section under wall errors. If it is required to extend the mainlobe further than that achievable by DC, second-order derivative constraints (SDC) can be added such that,

$$\mathbf{B} = [\mathbf{a}(m, n) \quad \nabla \mathbf{a}(m, n) \cdot \mathbf{v}_{m,n} \quad \nabla^2 \mathbf{a}(m, n) \cdot \mathbf{v}_{m,n}], \quad \mathbf{c} = \begin{bmatrix} 1 \\ 0 \\ 0 \end{bmatrix}. \quad (54)$$

One disadvantage of the derivative constrained methods (both DC and SDC) is that the extent of the mainlobe is limited and it may not cover the bias in target location resulting from large errors in wall parameters. One solution to extend the mainlobe along longer displacement trajectories is to use multiple consecutive unit-gain constraint (MC) beamforming, i.e.,

$$\mathbf{B} = [\mathbf{a}(m_0, n_0) \quad \mathbf{a}(m_1, n_1) \quad \dots \quad \mathbf{a}(m_T, n_T)], \quad \mathbf{c} = \begin{bmatrix} 1 \\ 1 \\ \vdots \\ 1 \end{bmatrix}, \quad (55)$$

where the points  $(m_0, n_0), \dots, (m_T, n_T)$  are located along a line whose center is at  $(m, n)$  and its slope is the same as that of  $\mathbf{v}_{m,n}$ . The extent of the mainlobe of MC is somewhat controllable by applying different number of constraints. However, at the same time, it is uncontrollable since it is determined by several variables, such as the number of antennas, location of targets, noise, and interference signals. Therefore, MC is most suitable to localize targets at their true locations when the targets are sparsely distributed in the scene.

It is interesting to consider the most recent proposed techniques for robust beamforming, including those in [26] to ensure high intensity image at and around the correct target positions. In this case, the linear and derivative constraints of equations (50) will be replaced by quadratic constraints with inequality which depend on an ellipsoid that describes errors. However, the advantages of these methods, although evident in passive arrays, are not significant in the underlying imaging applications. The reason is two-fold. First, the possible ripple behavior of the active array response between the unit constraint values of (53) is tolerable for the problem at hand. Unlike many robust beamforming techniques that are only concerned with guaranteed beamforming gain around the beamforming point in the desired direction, the underlying through-the-wall radar imaging problem requires an extension of the mainlobe without imposing the stringent requirement of a flat behavior. A priority in this problem is to limit the value of the beamforming gain outside the mainlobe extent. The proposed use of the multiple unit gain constraints satisfactorily achieves both these objectives. Second, the image pixels along and near the bias trajectory do not necessarily translate into an ellipsoid in the array manifold space. Unlike the errors in conventional robust beamforming techniques, the underlying problem deals with errors (biases) which can be predicted in the image domain and we can not guarantee that those biases in the image domain can be defined by tight ellipsoid in the array manifold space.

### C. Number of computations

The computational complexity of the MC MVDR beamformer can be approximated as follows. The solution to the constrained optimization problem of eq.(50) is given by [25],

$$\mathbf{w} = \mathbf{R}^{-1}\mathbf{B}(\mathbf{B}^H\mathbf{R}^{-1}\mathbf{B})^{-1}\mathbf{c}. \quad (56)$$

which leads to

$$\mathbf{w}^H\mathbf{R}\mathbf{w} = \mathbf{c}^H(\mathbf{B}^H\mathbf{R}^{-1}\mathbf{B})^{-1}\mathbf{c}. \quad (57)$$

In the above equation,  $\mathbf{R}^{-1}$  and  $\mathbf{c}$  are independent of the pixel being imaged and thus need to be computed once. On the other hand,  $\mathbf{B}$  varies from pixel to pixel and thus, the above equation will be computed for each pixel. The dimensions of the matrices  $\mathbf{c}$ ,  $\mathbf{B}$ , and  $\mathbf{R}$  are  $T \times 1$ ,  $MN \times T$ , and  $MN \times MN$ , respectively, where  $T$  is the number of constraints and  $MN$  is the length of the steering vector. The computational complexity of (57) is primarily associated with the computation of the inverse of the  $T \times T$  matrix  $\mathbf{B}^H\mathbf{R}^{-1}\mathbf{B}$ . The number of computations for the

inversion of the matrix  $\mathbf{B}^H \mathbf{R}^{-1} \mathbf{B}$  is  $O(T^3)$  [27]. Therefore, the number of computations for the MC MVDR beamformer can be approximated as

$$\eta_{MC} \approx N_u \cdot O(T^3) + O(M^3 N^3) + O(N_u^3), \quad (58)$$

where  $N_u$  is the total number of pixels and  $O(M^3 N^3)$  is the number of computations required to invert  $\mathbf{R}$ . The last term in eq.(58) represents the number of computations required for DS beamforming wherein, for convenience, both the number of frequencies and the number of antenna locations are assumed to be equal to  $N_u$ .

In comparison, the total number of computations for the target localization method of [18], which requires DS beamforming to be performed multiple times using  $N_p$  different sets of wall parameter pairs, is applied, is given by

$$\eta_{DS} \approx N_p \cdot O(N_u^3). \quad (59)$$

Typically,  $N_u$  is several orders of magnitude higher than  $T$  and  $N_p$ , which implies that  $\eta_{MC}$  is much less than  $\eta_{DS}$ . Thus, the proposed method is computationally more efficient than the DS beamforming based method of [18].

### VIII. SIMULATIONS OF UNKNOWN WALL DATA

The proposed high-definition algorithm for imaging using two array positions is tested with synthesized and real data. The synthetic data set consists of signals reflected from point targets. Only one refraction path through the wall is considered, as depicted in Fig. 1. The images corresponding to the two array positions are independently processed by constrained MVDR beamforming and are combined using two simple pixel-by-pixel fusion methods, namely, magnitude multiplication [10]. Results using the DS beamforming based method of [18] are also presented for comparison. It is noted that although the images corresponding to the two array locations are depicted using sensor-specific coordinate systems, these images are transformed into a single coordinate system prior to fusion.

---

Insert Figure 19 Here

---

Figure 19 shows the schematic of the scene being simulated. Both array #1 and array #2 are 1.2m long with 0.02m antenna spacing. The thickness of the wall is 0.38m and the dielectric

constant is 7.0. A stepped-frequency signal from 2 to 3GHz with 5MHz step size is used. The stand off distance of the arrays from the walls is 1m and the distance between the wall and the center of the scene is 6m. Two point targets having the same reflection coefficient are located at  $(-0.988, 6.512)$ m and  $(-0.8, 5.5)$ m in the scene from array #1, respectively.

---

Insert Figure 20 Here

---

For the synthesized data set, we consider the imaging performance under 10% error in both wall parameters. Consequently, the assumed wall thickness takes the value 0.418m and the assumed dielectric constant is 7.7. A delay-and-sum beamformer with rectangular window is used to obtain DS images from array #1 and #2, shown in Figures 20(a) and 20(b), respectively. The number of pixels in the images is 11449 ( $107 \times 107$ ). For constrained MVDR beamforming, the size of the sub-matrices for virtual snapshots is  $13 \times 6$  and the dimension of the covariance matrix is  $78 \times 78$ . Multiple consecutive unit gain constraints have been tested. The 10% parameter errors are too large for the derivative constrained method to handle. The direction of the line between the beamforming point and the center of the array is used as that of biases in the simulation.

---

Insert Figure 21 Here

---

Figures 20(c) and 20(d) show respective images obtained using the constrained MVDR beamforming from array #1 and #2. It is noted that the imaged target locations are biased toward the center of the array. However, the targets are stretched by the extended mainlobe, according to the constraints. A total of seven linear constraints are used in this simulation. If more constraints are used, the extended mainlobe will make the two targets indistinguishable, when imaged from array #1. If the range of the wall parameter values is known, the number of constraints can be determined and will depend on the largest bias in the wall parameters. Note that in this simulation, we create a very challenging scenario to evaluate the proposed approach, where multiple targets are aligned along the bias direction. Figure 21 is a contour plot showing the trajectories of the imaged target locations from array #1 and array #2, generated using the DS beamforming based method of [18]. Eight different pairs of wall parameters are used for trajectory generation.



---

Insert Figure 22 Here

---

When the image from array #1 is combined with the corresponding image from array #2, the two targets become identifiable and are correctly located for the MC MVDR, as shown in Fig. 22(b). Figure 22(a) is the combined DS image corresponding to the wall parameters obtained by intersection of the trajectories in Fig. 21. Comparing Fig. 22(a) and Fig. 22(b), we observe that although both methods correctly localize the targets, the DS beamforming based image has higher sidelobe levels. Also, MC MVDR for the aforementioned simulation parameters is computationally more efficient than the DS based method of [18].

---

Insert Figure 23, 24, 25 Here

---

For the real data experiment, we collected data of the single dihedral scene of Section VI, from two different angles, namely 0 and 90 degrees, emulating imaging from the front and the side walls, respectively. The scene layout and system parameters are the same as described in Section VI. The downrange to the target is approximately 2.7m from array #1 and 1.9m from array #2. We used wall parameters with 20% error and the corresponding images using DS beamforming are shown in Figs. 23(a) and 23(b). Since the wall thickness and the dielectric constant are smaller than those for the synthesized data case, the bias in the target location is not as severe. For array #2, we observe strong reflections from multiple points on the dihedral, which can be attributed to the target orientation relative to array #2 (see Fig. 25(a)). Figures 23(c) and 23(d) show respective images using the constrained MVDR beamforming from array #1 and #2, whereas Figures 24(a) and 24(b) depict the imaged target location trajectories for DS beamforming using eight different pairs of wall parameters.

The combined MC MVDR image, shown in Fig. 25(c), correctly detects the presence of a single target and shows the imaged target at its true location. The image in Fig. 25(b) is the combined DS image, using parameters obtained by trajectory intersection for operation from array #1 and array #2. We observe that although the MC MVDR image has a slightly wider mainlobe than the DS image, the DS image has higher sidelobe levels.

## IX. CONCLUSION

The problem of high-definition through-the-wall imaging was considered. A new method, which provides accurate target locations using MVDR beamformer under exact and inaccurate wall parameter values, was proposed. Two approaches based on raw data and beamspace data were presented and compared in performance under near field and far field situations. It was concluded that using delay and sum beamformer image to produce the spatial spectrum, which is then used for covariance matrix estimation, is more robust to far field approximation and should be the preferred way to conduct indoor high definition imaging. When using the spatial spectrum, however, one must only consider the region which corresponds to the target, otherwise virtual snapshots obtained by subarray and subband vectors will not properly correspond to the array manifolds, leading to target image dispersion.

We have also analyzed the bias in imaged target location due to wall errors beyond that discussed in reference [18]. The bias results were then used to define additional constraints on MVDR beamformer which led to provide unbiased target location when imaging with different view angles. Simulated and real data were used in the paper and demonstrated the superior performance of the proposed technique compared to the commonly applied delay-and-sum beamforming.

## REFERENCES

- [1] F. Ahmad, M. Amin, and S. Kassam, "Synthetic aperture beamformer for imaging through a dielectric wall," *IEEE Trans. Aerosp. Electron. Syst.*, vol. 41, no. 1, pp. 271–283, Jan. 2005.
- [2] H. Yacoub and T. Sarkar, "Monostatic through-wall detection of a metallic sphere," in *Antennas and Propagation Society International Symposium*, July 2005.
- [3] F. Soldovieri and R. Solimene, "Through-wall imaging via a linear inverse scattering algorithm," *IEEE Geoscience and Remote Sensing Lett.*, vol. 4, no. 4, Oct. 2007.
- [4] E. Ertin and R. Moses, "Through-the-wall sar attributed scattering center feature estimation," in *Proc. IEEE Int. Conf. Acoustics, Speech, Signal Process.*, Apr. 2008.
- [5] R. Narayanan, "Through wall radar imaging using uwb noise waveforms," in *Proc. IEEE Int. Conf. Acoustics, Speech, Signal Process.*, Apr. 2008.
- [6] E. Lively, Y. Zhang, E. H. III, Y. Lai, P. Weichman, and A. Chapman, "Theoretical and experimental study of through-wall microwave tomography inverse problems," *Journal of the Franklin Institute*, vol. 345, no. 6, pp. 592–617, Sept. 2008.
- [7] M. Farwell, J. Ross, R. Luttrell, D. Cohen, W. Chin, and T. Dogaru, "Sense through the wall system development and design considerations," *Journal of the Franklin Institute*, vol. 345, no. 6, pp. 570–591, Sept. 2008.
- [8] L. Frazier, "Radar surveillance through solid materials," in *Proceedings of SPIE, Command, Control, Communications, and Intelligence Systems for Law Enforcement*, vol. 2938, Nov. 1997, pp. 139–146.

- [9] F. Ahmad, G. Frazer, S. Kassam, and M. Amin, "Design and implementation of near-field, wideband synthetic aperture beamformers," *IEEE Trans. Aerosp. Electron. Syst.*, vol. 40, no. 1, pp. 206–220, Jan. 2004.
- [10] F. Ahmad, Y. Zhang, and M. Amin, "Three-dimensional wideband beamforming for imaging through a single wall," *IEEE Geoscience and Remote Sensing Lett.*, vol. 5, no. 2, Apr. 2008.
- [11] G. Benitz, "High-definition vector imaging," *Lincoln Lab Journal*, vol. 10, no. 2, 1997.
- [12] J. Odendaal, E. Barnard, and C. Pistorius, "Two-dimensional superresolution radar imaging using the MUSIC algorithm," *IEEE Trans. Antennas Propagat.*, vol. 42, pp. 1386–1391, Oct. 1994.
- [13] G. Benitz, "High-definition imaging apparatus and method," U.S. Patent No. 6,608,585, Aug. 2003.
- [14] F. Ahmad and M. Amin, "High-resolution imaging using Capon beamformers for urban sensing applications," in *Proc. IEEE Int. Conf. Acoustics, Speech, Signal Process.*, Apr. 2007.
- [15] Y.-S. Yoon and M. Amin, "High-resolution through-the-wall radar imaging using beamspace MUSIC," *IEEE Trans. Antennas Propagat.*, vol. 56, no. 6, pp. 1763–1774, June 2008.
- [16] F. Ahmad, M. Amin, and G. Mandapati, "Autofocusing of through-the-wall radar imagery under unknown wall characteristics," *IEEE Trans. Image Processing*, vol. 16, no. 7, pp. 1785–1795, July 2007.
- [17] M. Dehmollaian and K. Sarabandi, "Analytical, numerical, and experimental methods for through-the-wall radar imaging," in *Proc. IEEE Int. Conf. Acoustics, Speech, Signal Process.*, Apr. 2008, pp. 5181–5184.
- [18] G. Wang and M. Amin, "Imaging through unknown walls using different standoff distances," *IEEE Trans. Signal Processing*, vol. 54, no. 10, pp. 4015–4025, Oct. 2006.
- [19] F. Ahmad and M. Amin, "Noncoherent approach to through-the-wall radar localization," *IEEE Trans. Aerosp. Electron. Syst.*, vol. 42, no. 4, pp. 1405–1419, Oct. 2006.
- [20] M. Dehmollaian and K. Sarabandi, "Refocusing through building walls using synthetic aperture radar," *IEEE Trans. Geosci. Remote Sensing*, vol. 46, no. 6, June 2008.
- [21] Y.-S. Yoon and M. Amin, "Spatial filtering for wall-clutter mitigation in through-the-wall radar imaging," *IEEE Trans. Geosci. Remote Sensing*, 2009, under review.
- [22] R. Schmidt, "Multiple emitter location and signal parameter estimation," *IEEE Trans. Antennas Propagat.*, vol. AP-34, no. 3, pp. 276–280, Mar. 1986.
- [23] J. Capon, "High-resolution frequency wavenumber spectrum analysis," *Proc. IEEE*, vol. 57, no. 8, pp. 1408–1411, 1969.
- [24] F. Ahmad and M. Amin, "Multi-location wideband synthetic aperture imaging for urban sensing applications," *Journal of the Franklin Institute*, vol. 345, no. 6, pp. 618–639, Sept. 2008.
- [25] D. Johnson and D. Dudgeon, *Array Signal Processing: Concepts and techniques*. Englewood Cliffs, NJ: Prentice Hall, 1993.
- [26] J. Li and P. Stoica, *Robust Adaptive Beamforming*. Hoboken, NJ: John Wiley, 2006.
- [27] G. Golub and C. V. Loan, *Matrix Computations*. Baltimore, MD: Johns Hopkins University Press, 1996.

PLACE  
PHOTO  
HERE

**Yeo-Sun Yoon** - (S'02-M'05) received the B.S. degree from Yonsei University, Seoul, Korea, in 1995 and the M.S. degree from the University of Michigan, Ann Arbor, in 1998 and the Ph.D. degree from the Georgia Institute of Technology, Atlanta, in 2004, all in electrical engineering.

From 1999 to 2004, he was a Graduate Research Assistant in the Center for Signal and Image Processing (CSIP) at the Georgia Institute of Technology. In the summer, from 2000 to 2002, he worked as a Research Assistant at the Center for Theoretical Studies of Physical Systems (CTSPS), Atlanta, in a co-op program. He has been a senior engineer at the Samsung Thales Company, Ltd., Yongin, Korea since 2004. From 2007 to 2009, he was a Post-doctoral research fellow at the Center for Advanced Communications (CAC), Villanova University, Villanova, PA.

His research interests include array signal processing, high-resolution radar imaging, signal parameter estimation, and compressive sensing for radar.

PLACE  
PHOTO  
HERE

**Moeness G. Amin** - (S'82-M'83-SM'91-F'01) received his Ph.D. degree in 1984 from University of Colorado, Boulder. He has been on the Faculty of Villanova University since 1985, where is now a Professor in the Department of Electrical and Computer Engineering and the Director of the Center for Advanced Communications.

Dr. Amin is the recipient of the 2009 Individual Technical Achievement Award from the European Association of Signal Processing. He is a Fellow of the Institute of Electrical and Electronics Engineers (IEEE); Fellow of the International Society of Optical Engineering; Recipient of the IEEE Third Millennium Medal; Distinguished Lecturer of the IEEE Signal Processing Society for 2003 and 2004; Member of the Franklin Institute Committee on Science and the Arts; Recipient of the 1997 Villanova University Outstanding Faculty Research Award; Recipient of the 1997 IEEE Philadelphia Section Service Award.

Dr. Amin has over 400 publications in the areas of Wireless Communications, Time-Frequency Analysis, Smart Antennas, Interference Cancellation in Broadband Communication Platforms, Direction Finding, GPS Technologies, Over the Horizon Radar, and Radar Imaging. He was a Guest Editor of the Journal of Franklin Institute September-08 Special Issue on Advances in Indoor Radar Imaging. He is a Guest Editor of the IEEE Transactions on Geoscience and Remote Sensing May-09 Special issue on Remote Sensing of Building Interior. Dr. Amin is the Co-Guest editor of IET Signal Processing upcoming Special Issue on Time-Frequency Approach to Radar Detection, Imaging, and Classification.

Dr. Amin was the Co-Chair of the Special Sessions of the 2008 IEEE International Conference on Acoustics, Speech, and Signal Processing, Nevada. He was the Technical Chair of the 2nd IEEE International Symposium on Signal Processing and Information Technology, Morocco, 2002; The General and Organization Chair of the IEEE Workshop on Statistical Signal and Array Processing, Pennsylvania, 2000.; The General and Organization Chair of the IEEE International Symposium on Time-Frequency and Time-Scale Analysis, Pennsylvania, 1994. He was an Associate Editor of the IEEE Transactions on Signal Processing during 1996-1998. Dr. Amin was a member of the IEEE Signal Processing Society Technical Committee on Signal Processing for Communications during 1998-2002 and was a Member of the IEEE Signal Processing Society Technical Committee on Statistical Signal and Array Processing during 1995-1997

PLACE  
PHOTO  
HERE

**Fauzia Ahmad** - (S'97-M'97-SM'06) received her MSEE degree in Electrical Engineering in 1996, and Ph.D. degree in Electrical Engineering in 1997, both from the University of Pennsylvania, Philadelphia, PA.

From 1998 to 2000, she was an Assistant Professor in the College of Electrical and Mechanical Engineering, National University of Sciences and Technology, Pakistan. During 2000-2001, she served as an Assistant Professor at Fizaia College of Information Technology, Pakistan. Since 2002, she has been with the Center for Advanced Communications, Villanova University, Villanova, PA, where she is now a Research Associate Professor and the Director of the Radar Imaging Lab.

Dr. Ahmad has several journal and conference publications in the areas of radar imaging, array signal processing, sensor networks, and image processing.

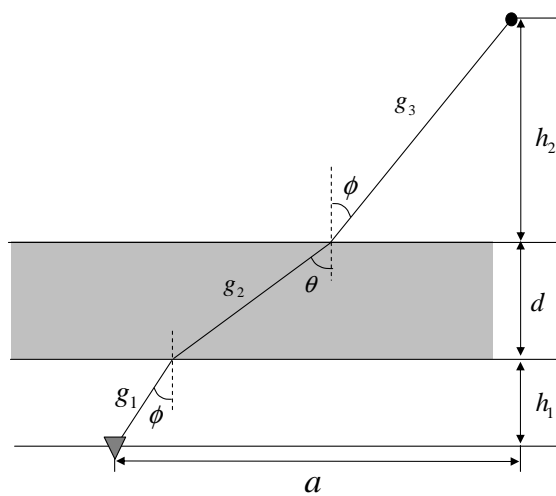


Fig. 1: Signal path with a wall

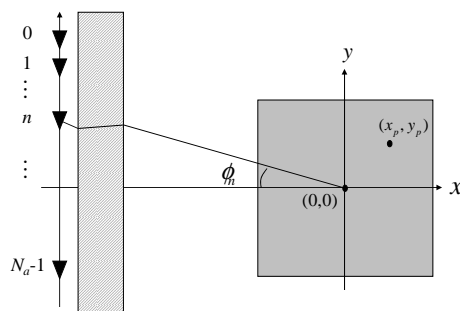


Fig. 2: Signal propagation through the wall.

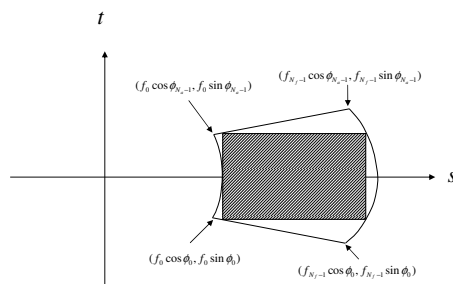


Fig. 3: Bound of spatial frequency of the raw data approach.

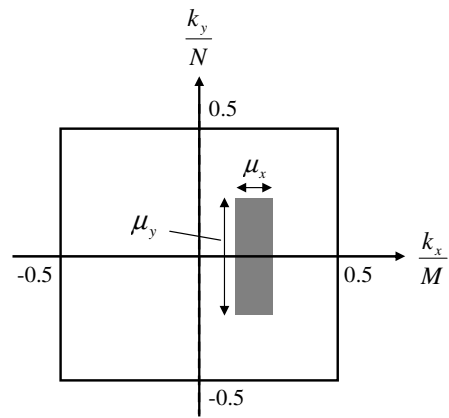


Fig. 4: Two-dimensional spatial spectrum of the DS image.

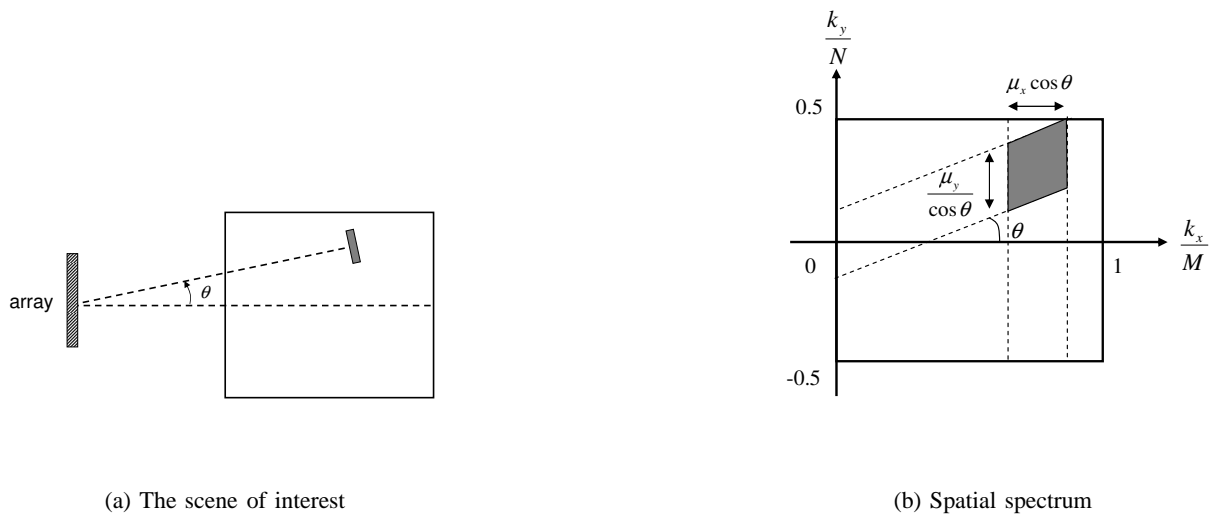


Fig. 5: The scene of interest of the off-boresight target and corresponding spatial spectrum.

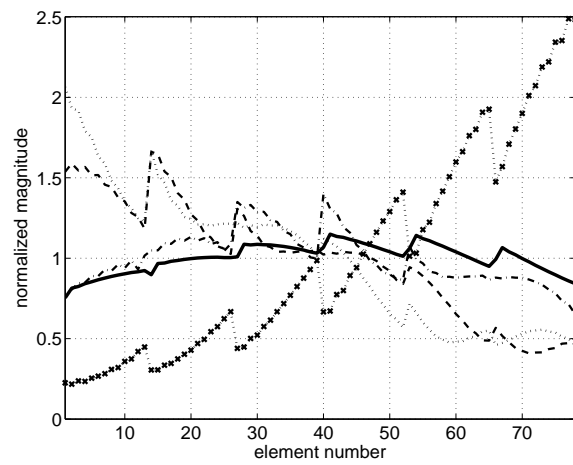


Fig. 6: Normalized magnitudes of the elements of the steering vector after averaging (solid line) and those of virtual snapshots (dotted lines).

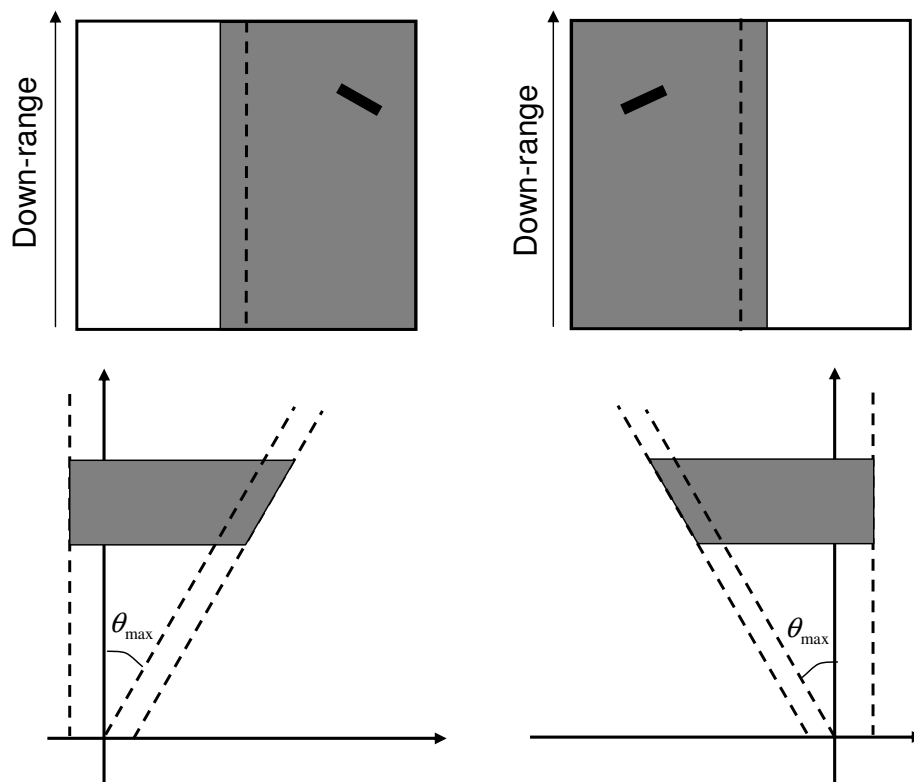


Fig. 7: Two tiles of the scene and their corresponding spatial spectrum. The left column is for negative  $\theta$  and the right column is for positive  $\theta$ .



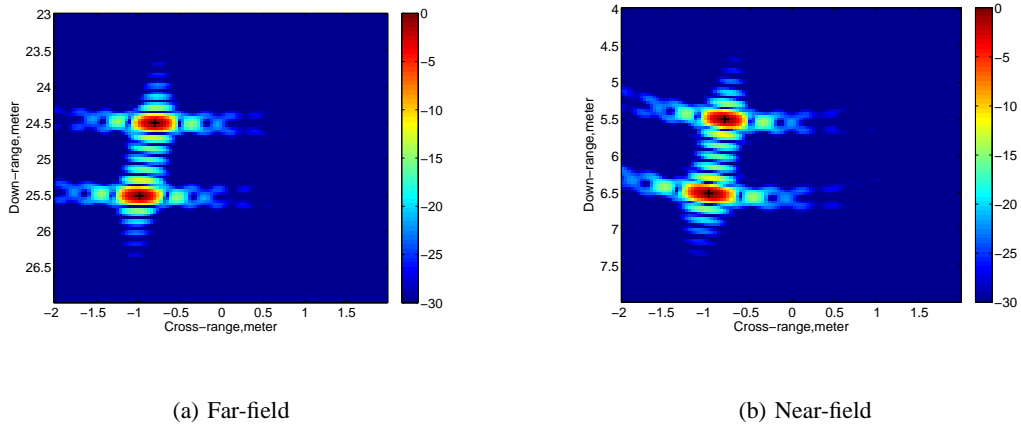


Fig. 8: Delay-and-sum beamforming. (a) Far-field and (b) near-field.

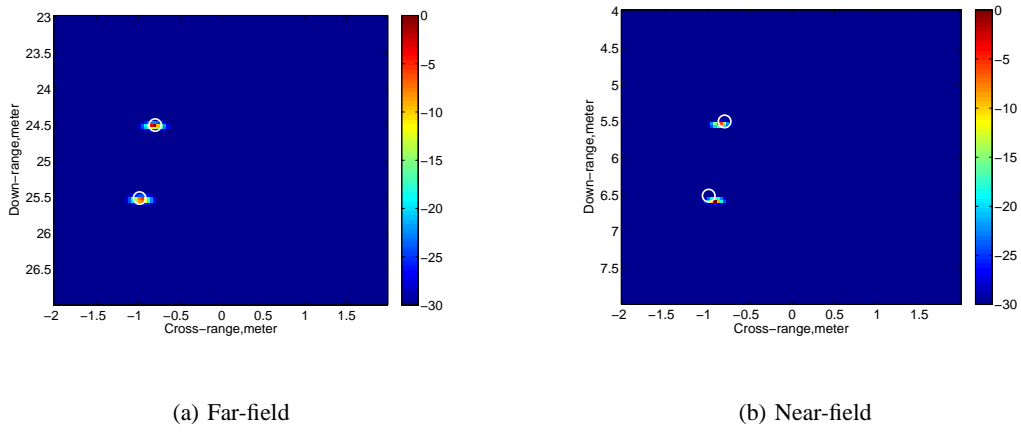


Fig. 9: Raw data-based Capon. (a) Far-field and (b) near-field.

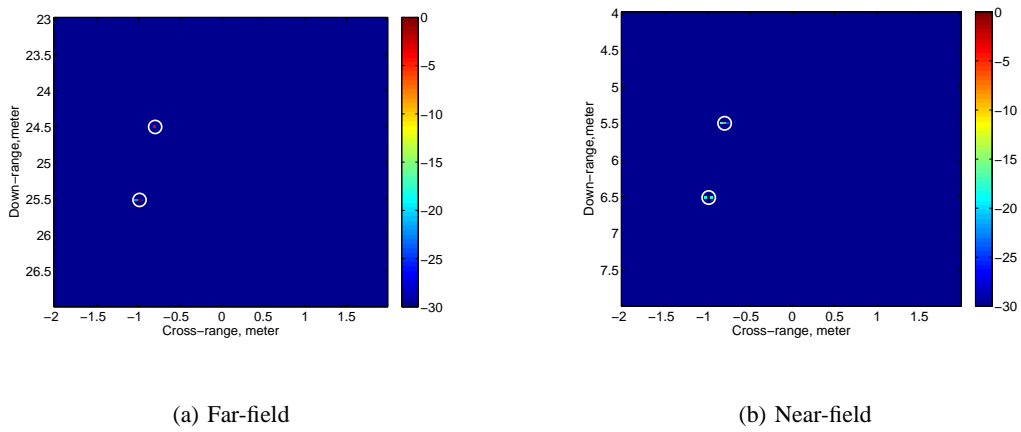


Fig. 10: Beam-space-based Capon. (a) Far-field and (b) near-field.

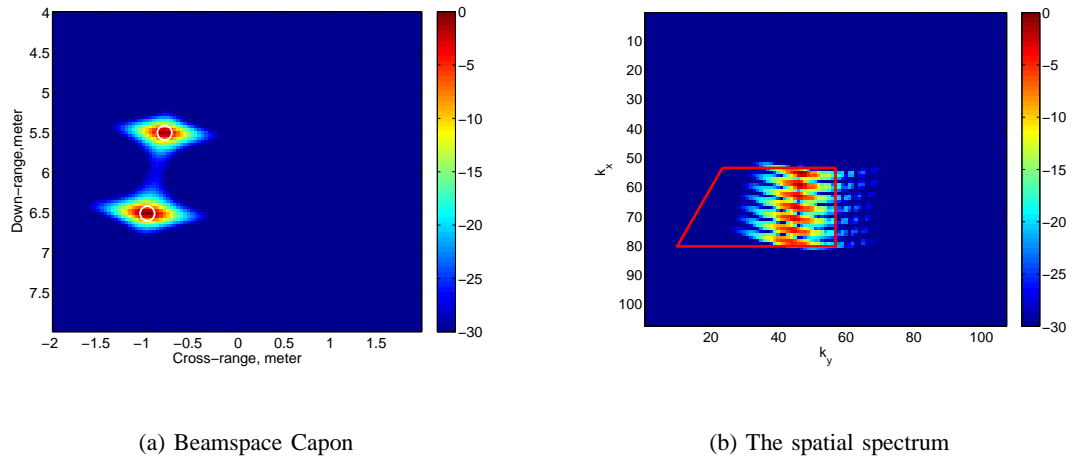


Fig. 11: Beamspace-based Capon. (a) the beamspace Capon image using the entire spatial spectrum and (b) the corresponding 2D spatial spectrum. The red boundary indicates the area used for the covariance matrix estimation in Fig. 10.

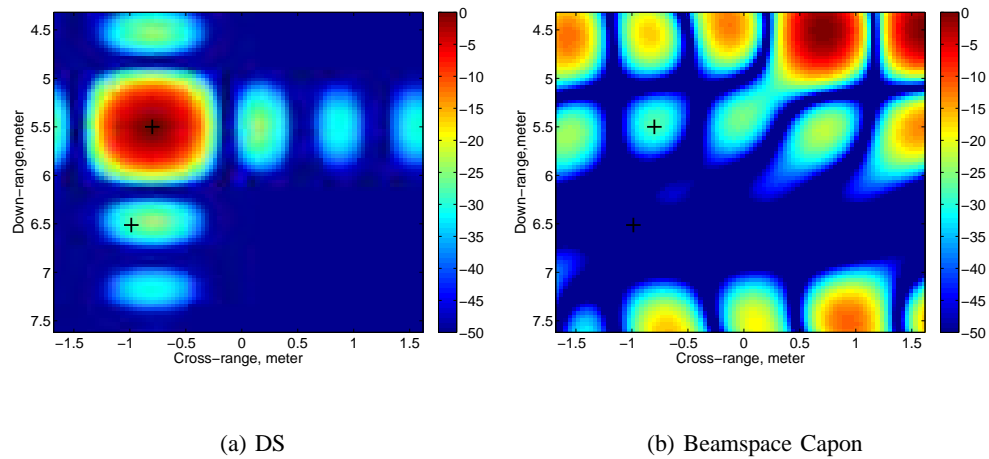


Fig. 12: Spatial leakage patterns for DS and beamspace Capon beamformers when the beamforming point is at  $(-0.8, 5.5)$ .

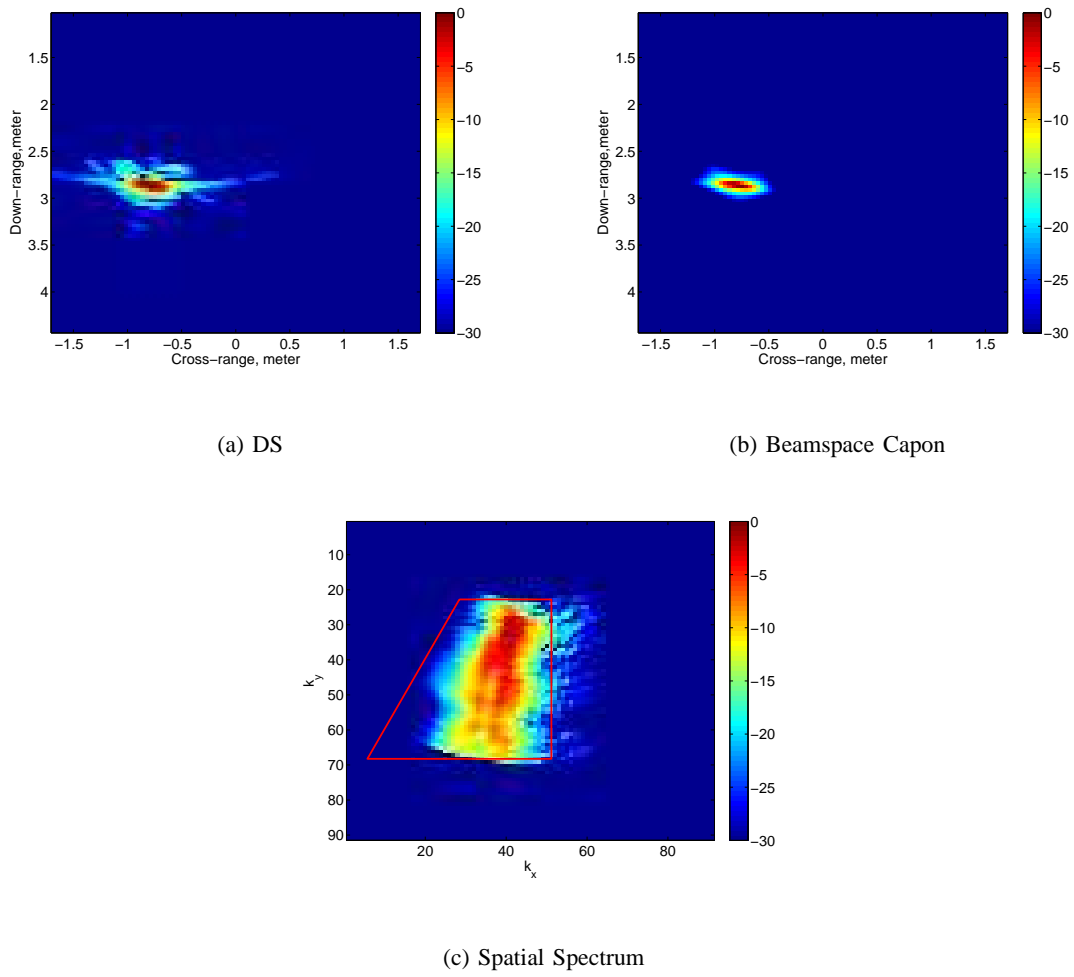


Fig. 13: Results of the experiment data. (a) Delay-and-sum, (b) Beamspace-based Capon, and (c) the corresponding spatial spectrum.

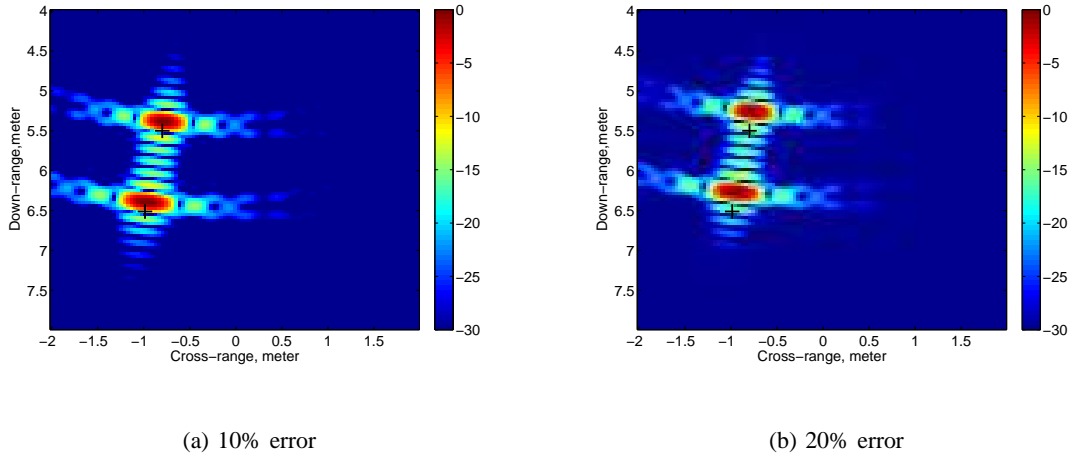


Fig. 14: Images of the two-target scene with errors in the wall parameters. (a) with 10% error and (b) with 20% error

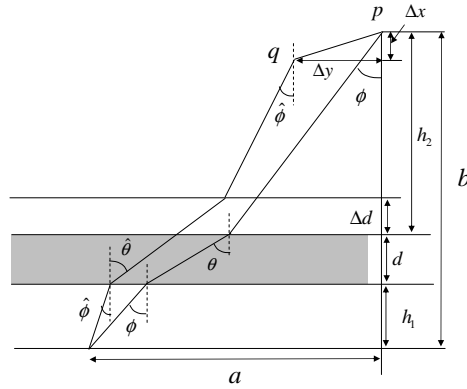


Fig. 15: Geometry of the through-the-wall radar under wall parameter errors.

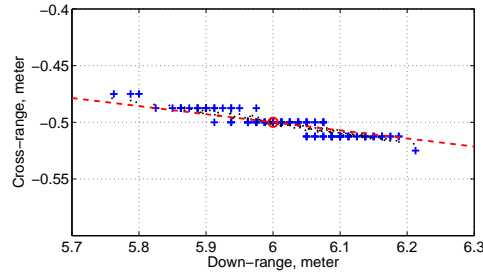


Fig. 16: Biases due to wrong wall parameters. The circle indicates the true target location. Crosses and dots represent biases from numerical simulations, and from computation, respectively. The dashed line connects the center of the array and the target location.

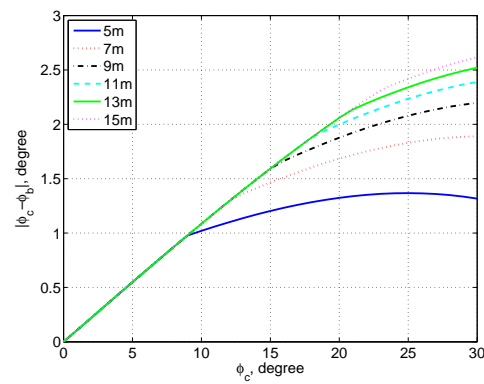


Fig. 17: Differences between  $\phi_c$  and  $\phi_b$ . For different distances between the center of the array and the target location.

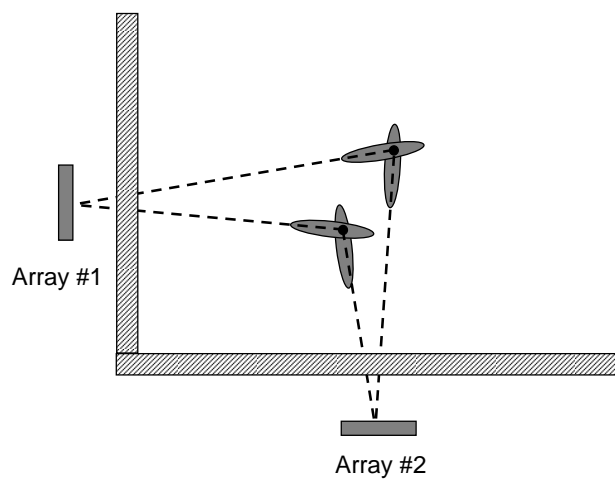


Fig. 18: Superposition of constrained MVDR images corresponding to two different array positions.

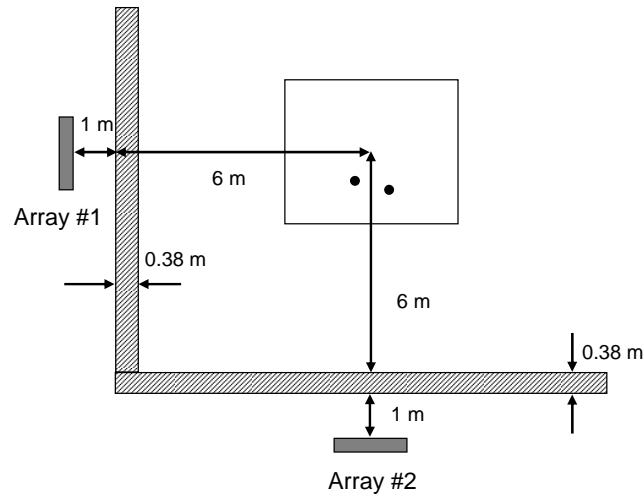


Fig. 19: Radar geometry for the simulation.

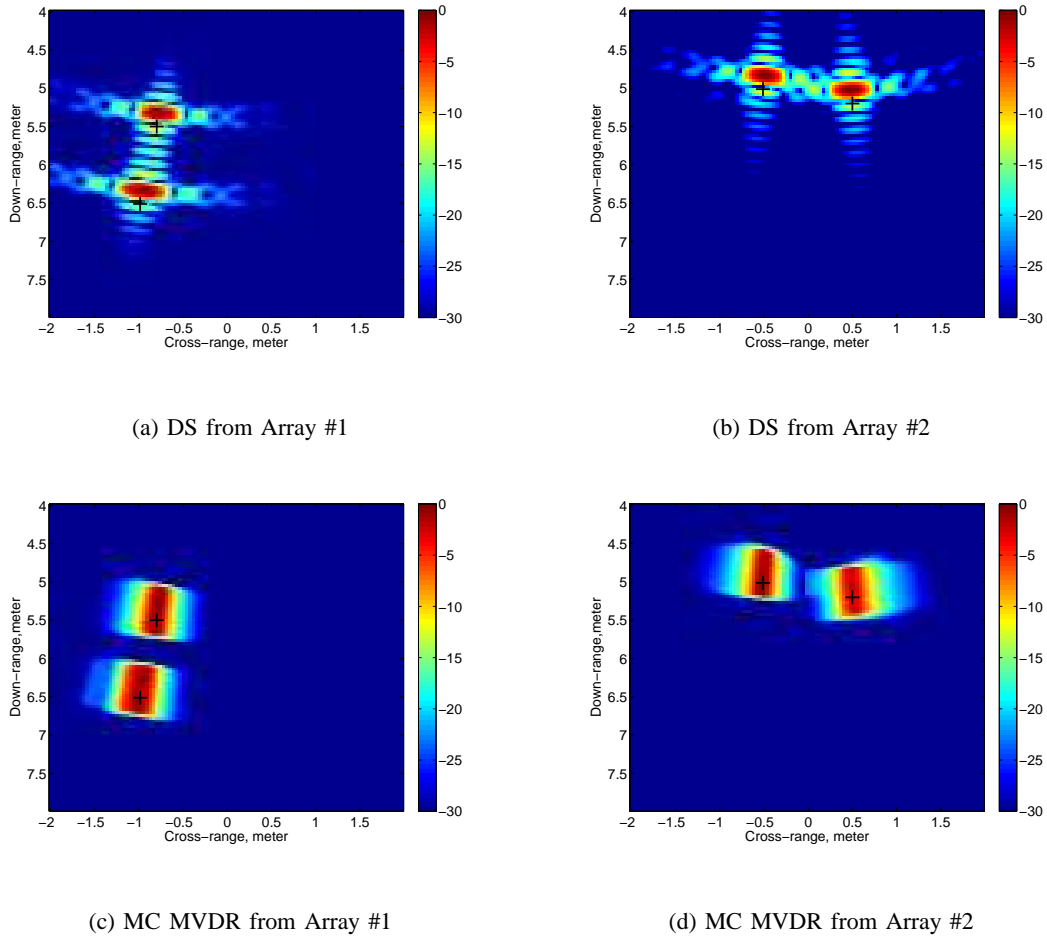


Fig. 20: Images of the synthesized two-target scene with 10% errors in the wall parameters.

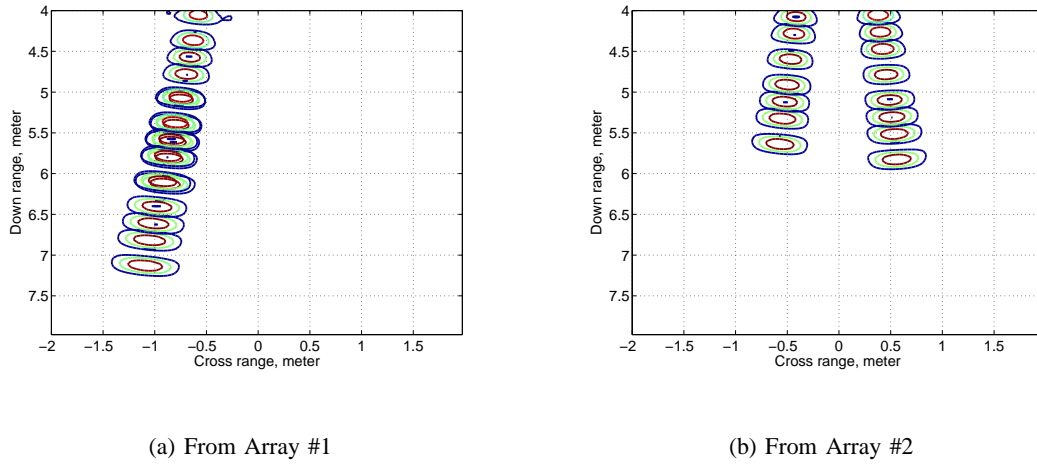


Fig. 21: Trajectories of imaged target locations for DS images using multiple pairs of wall parameters.

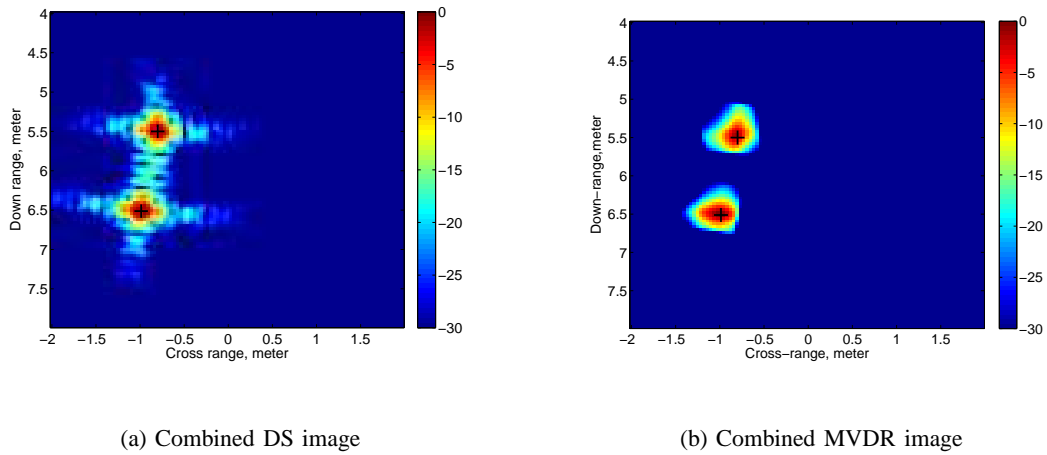
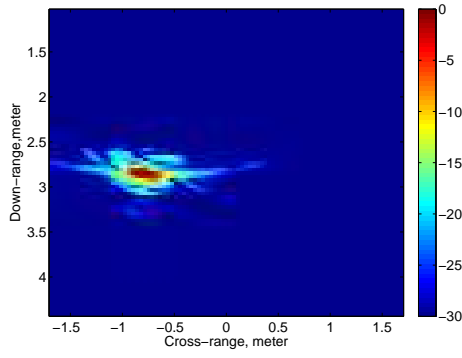
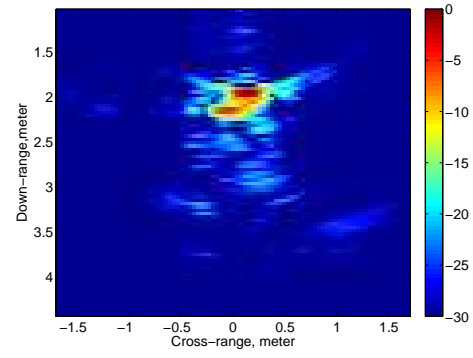


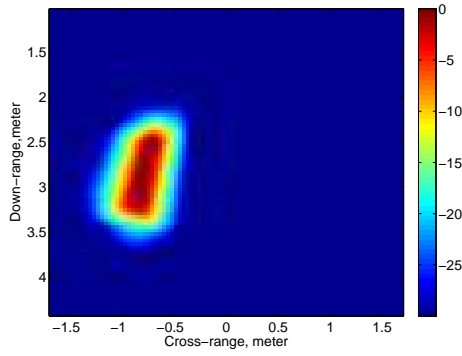
Fig. 22: Combined images. (a) combined DS images using wall parameters estimated from trajectory intersection.  
(b) combined MVDR images when there is 10% errors in the wall parameters



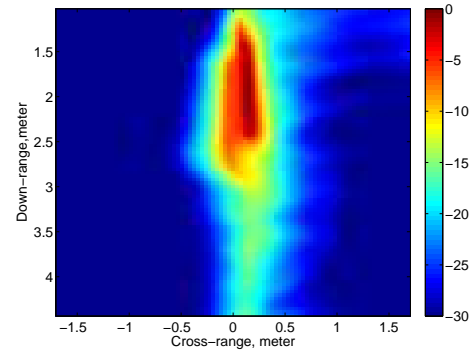
(a) DS from Array #1



(b) DS from Array #2

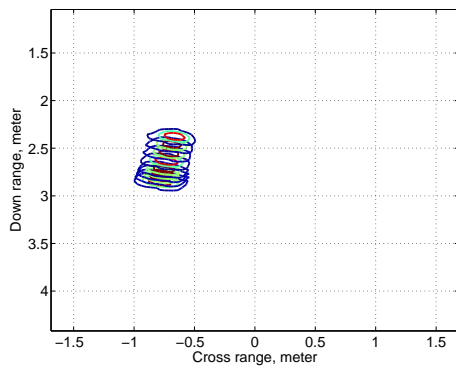


(c) MC MVDR from Array #1

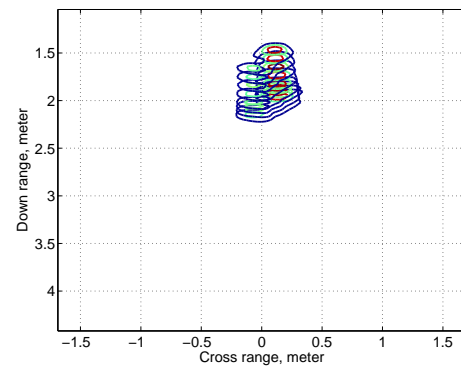


(d) MC MVDR from Array #2

Fig. 23: Images of the real scene with 20% errors in the wall parameters.



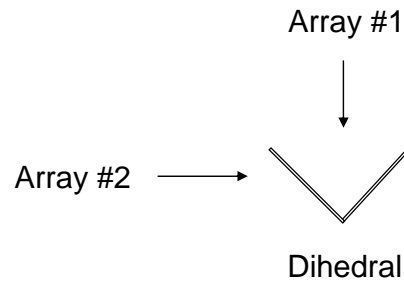
(a) From Array #1



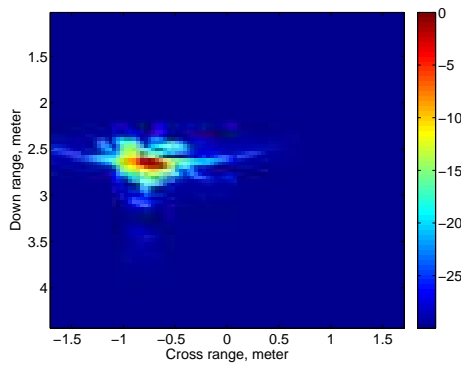
(b) From Array #2

Fig. 24: Trajectories of imaged target locations for DS images using multiple pairs of wall parameters.

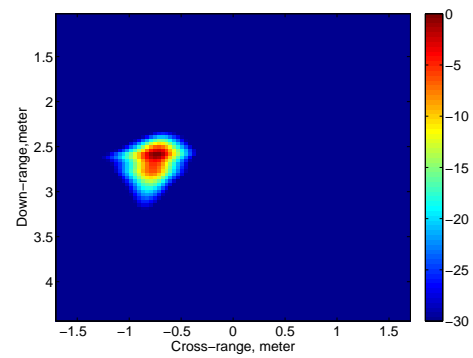




(a) Target orientation relative to array #1 and #2



(b) Combined DS image



(c) Combined MVDR image

Fig. 25: (a) Target orientation. (b) Combined image using DS beamforming based method of [18]. (b) combined image using MVDR when there is 20% errors in the wall parameters.